Ru₁Coₙ Single-Atom Alloy for Enhancing Fischer−Tropsch Synthesis

Ge Meng,[∇] Jiaqiang Sun,[∇] Lei Tao,[∇] Kaiyue Ji, Pengfei Wang, Yu Wang,* Xiaohui Sun, Tingting Cui, Shixuan Du, Jiangang Chen,* Dingsheng Wang, and Yadong Li*

ACCESS | 📊 Metrics & More | 📰 Article Recommendations | Ⓢ Supporting Information

ABSTRACT: Fischer−Tropsch synthesis (FTS) is a significant catalytic process for the production of liquid fuel and fine chemicals from natural gas-, coal-, and biomass-derived syngas. However, exploring high-performance catalysts and understanding the catalytic mechanism remain challenging. Herein, we design a Ru₁Coₙ single-atom alloy (SAA) catalyst with isolated Ru atoms anchored onto a Co nanoparticle surface through a two-dimensional confinement strategy to achieve greatly improved FTS activity (2.6 mol_{CO} mol_M^{-1} h^{-1}) and long-chain hydrocarbon selectivity (C_{5^+}: 86.0%) at a low reaction temperature of 150 °C. A series of *in situ* experiments, catalytic tests, and density functional theory (DFT) calculations reveal that the Ru single-atom sites in Ru₁Coₙ SAA are more active for the FTS reaction than pure Ru and Co surfaces. This is because single-atom Ru with a much higher electronic density near the Fermi level could effectively and simultaneously decrease the rate-limiting barriers of both C−O splitting and chain growth processes. This work demonstrates the possibility of designing Ru single-atom sites to improve FTS performance and provides a deeper understanding of the strategy for developing other high-performance industrial catalysts.

KEYWORDS: *Fischer−Tropsch synthesis, RuCo catalyst, single-atom alloy, in situ study, two-dimensional confinement strategy*
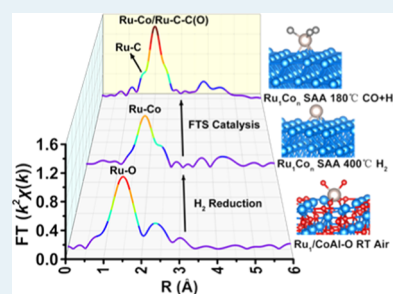
1. INTRODUCTION

Fischer−Tropsch synthesis (FTS) is a key technology in the production of sulfur- and nitrogen-free fuels and high-value chemicals from multitudinous nonpetroleum feedstocks (*e.g.*, natural gas, coal, and biomass) through syngas (CO/H₂)-mediated chemical conversions.[1−8] Among the widely used FTS catalysts, Co and Ru catalysts have attracted substantial attention due to their higher long-chain paraffin productivity, longer durability, and lower working temperature (180−240 °C) compared to Fe-based catalysts.[1,9−20] In recent years, researchers have made great effort in designing Co/Ru catalysts to improve their FTS performance, including optimizing the particle size,[21−27] enhancing reducibility,[28−34] regulating the crystal phase,[35−39] *etc*. However, it remains a great challenge to promote CO hydrogenation reactivity, long-chain hydrocarbon selectivity, and long-term stability for widespread commercialization. Moreover, it is critical but arduous to identify the structure of reactive sites during FTS *via in situ* spectroscopy techniques and density functional theory (DFT) calculations to understand the catalytic mechanism and guide the catalyst design at the atomic level.

Recently, single-atom site catalysts, including single-atom alloys (SAAs), with the features of maximum utilization of the metal atoms,[40−44] uniform active sites,[45−48] and peculiar geometric and electronic structures,[49−53] have exhibited unique catalytic behavior for multitudinous heterogeneous reactions.[54−59] This concept has provided new opportunities for exploring high-performance FTS catalysts. The superiority of uniform and well-defined active centers in SAA catalysts is also highly beneficial for studying the catalytic mechanism and structure−activity relationship in FTS reactions. Nevertheless, SAA catalysts have never been applied in FTS to date due to the difficulty in maintaining the isolation of single atoms against aggregation under a thermal treatment during their preparation or catalytic process.

Herein, we provide a strategy of layered double hydroxide (LDH)-based anion intercalation and two-dimensional (2D) confinement to synthesize a thermally stable and high-performance Ru₁Coₙ SAA catalyst for an FTS reaction. The formation and catalytic mechanism of Ru₁Coₙ SAA were thoroughly studied by a series of *in situ* spectroscopy tests, catalytic experiments, and DFT calculations. It was indicated that Ru single-atom sites on Ru₁Coₙ SAA can facilitate both CO splitting and chain growth processes, resulting in a high catalytic activity and a heavy hydrocarbon selectivity at a low temperature. This work offers an efficient strategy for designing SAA catalysts with high reactivity and the economic benefit of low precious metal consumption for FTS and other industrial catalytic systems.

2. EXPERIMENTAL SECTION

2.1. Reagents. Potassium pentachloroaquaruthenium(III) (99.99%, Alfa Aesar), cobalt(II) nitrate hexahydrate (99%, Alfa Aesar), aluminum(III) nitrate nonahydrate (99%, Alfa Aesar), sodium hydroxide (Beijing Chemical Reagents, P. R. China), ruthenium(III) nitrosyl nitrate (Ru 31%, Alfa Aesar), and poly(N-vinyl-2-pyrrolidone) (PVP, molecular weight (MW) = 10 000, Alfa Aesar) were used without further purification.

2.2. Synthesis of Ru$_1$/CoAl−O and CoAl−O Samples. Ru$_1$/CoAl−O was prepared via an LDH 2D confinement strategy. First, RuCl$_5^{2-}$ intercalated CoAl-LDHs (referred to as CoAl-(RuCl$_5^{2-}$)-LDHs) were prepared using a coprecipitation process.[60] Typically, 16 mmol of Co(NO$_3$)$_2$·6H$_2$O and 5.33 mmol of Al(NO$_3$)$_3$·9H$_2$O were dissolved in a beaker with 20 mL of deionized water to form a clarified pink solution. Then, 34.15 mmol of NaOH and 0.05 mmol of K$_2$RuCl$_5$ were dissolved in 20 mL of deionized water to form a clarified solution in another beaker. Afterward, the as-prepared two solutions were simultaneously added dropwise into 40 mL of deionized water with magnetic stirring at 600 rpm. The solution was maintained at a pH value of 8.5 during titration by virtue of a pH indicator. After titration, the mixed liquid was stirred for another 12 h and the brown product was collected and washed via centrifugation at 10 000 rpm with ethanol and water alternately four times. The product was then dried at 80 °C for at least 4 h and ground to a brown powder.

Then, the thermal reduction of as-prepared CoAl-(RuCl$_5^{2-}$)-LDHs was conducted in a tube furnace under a 5% H$_2$/N$_2$ atmosphere at 400 °C for 3 h. Afterward, the powder was collected under an air atmosphere, during which the metallic Co and Ru species were reoxidized by O$_2$ to form a Ru$_1$/CoAl−O sample. CoAl−O was prepared with a synthetic procedure similar to that of Ru$_1$/CoAl−O, but without the addition of K$_2$RuCl$_5$.

2.3. Synthesis of Ru Nanoparticles (NPs)/CoAl−O. First, Ru nanoparticles were prepared according to a previously reported method.[61] Typically, ethylene glycol solutions of Ru(NO)(NO$_3$)$_3$ (7 mL, 10 mg mL^{-1}), PVP (224 mg, MW = 30 000), and ethylene glycol (193 mL) were mixed in a 500 mL mouth flask to form a homogeneous solution under stirring, followed by heating and refluxing at 200 °C for 3 h in air. The as-obtained Ru nanoparticles were collected and washed with an ethanol−acetone mixture through centrifugation and redispersed in 20 mL of ethanol. Subsequently, ∼3 mg of the resulting Ru NPs and 1 g of the as-prepared CoAl−O were dispersed in 40 mL of ethanol under stirring for 6 h. The product was then collected via centrifugation and dried at 60 °C for 4 h. To remove the surfactants (PVP) adsorbed on the surface of Ru NPs, the obtained compounds were calcined at 200 °C for 4 h under an air atmosphere and further thermally reduced at 400 °C under a 5% H$_2$/N$_2$ atmosphere for 3 h. Similarly, the final product was collected and reoxidized via O$_2$ in air, forming a Ru NPs/CoAl−O sample.

2.4. Characterizations. Transmission electron microscopy (TEM) images of the samples were obtained on a Hitachi H-800 TEM operated at 100 kV. High-resolution TEM (HRTEM) images were obtained on an FEI Tecnai G2 F20 S-Twin high-resolution TEM operated at 200 kV. Aberration-corrected high-angle annular dark-field scanning transmission electron microscopy (AC-HAADF-STEM) images were obtained using an ARM-200CF (JEOL, Tokyo, Japan) transmission electron microscope operated at 300 kV and

equipped with double-spherical aberration (Cs) correctors. The attainable resolution of the probe defined by the objective prefield is 78 pm. The Ru, Co, and Al concentrations were collected on inductively coupled plasma optical emission spectrometry (ICP-OES). The Cl and K concentrations were measured via X-ray fluorescence (XRF) analysis on an S4 Pioneer X-ray fluorescence spectrometer. N$_2$ adsorption−desorption and Brunauer−Emmett−Teller (BET) experiments were carried out on an Autosorb-IQ2-MP Instrument.

Hydrogen temperature-programmed reduction (H$_2$-TPR) experiments were conducted with a Micromeritics AutoChem II unit. The sample (60 mg) was placed in a quartz tubular reactor and reduced using 5% H$_2$/N$_2$ gas mixture at a flow rate of 50 mL min^{-1}. The temperature was raised at a rate of 10 °C min^{-1} from 50 to 850 °C. A thermal conductivity detector (TCD) was used to determine the hydrogen consumption. The degree of reduction (DOR) was measured using a TPR approach. The samples were heated to 400 °C at a rate of 10 °C min^{-1} and held there for 6 h. The reduced cobalt was measured based on the amount of hydrogen consumed in the reduction process using CuO as a standard. The DOR was then calculated by dividing the amount of reduced cobalt by the total cobalt content from the ICP-OES results.

In situ powder X-ray diffraction (PXRD) experiments were performed on a Bruker D8 Advance that provided Cu Kα radiation (λ = 1.5418 Å). The sample (300 mg) packed on a sintered glass sieve was placed in the center of the *in situ* cell. In this cell, the sample was reduced using H$_2$ at a flow rate of 50 mL min^{-1}. The temperature was raised at a rate of 2 °C min^{-1} from 25 to 400 °C. The PXRD patterns were recorded *in situ* under gas flows at desired temperatures. The measuring time per PXRD pattern in the 2θ range between 5 and 85° was 40 min.

In situ X-ray photoelectron spectroscopy (XPS) studies were performed on a Kratos Axis Ultra DLD. The sample was placed into an *in situ* cell and reduced using H$_2$ with a flow rate of 50 mL min^{-1} at 400 °C for 6 h. The XPS tests were conducted under air isolation conditions after the temperature naturally decreased to room temperature.

Hydrogen temperature-programmed desorption (H$_2$-TPD) tests were used to estimate the number of surface metal sites of the three catalysts using a Micromeritics AutoChem 2920 system. The catalysts (80 mg) (Ru$_1$/CoAl−O, Ru NPs/CoAl−O and CoAl−O) were first reduced at 400 °C for 6 h under a flow of high-purity hydrogen (flow rate = 30 mL min^{-1}) to obtain Ru$_1$Co$_n$ SAA, Ru/Co NPs and Co NPs samples, respectively. Then, the samples were cooled to 50 °C and saturated with H$_2$. After removing the physically adsorbed H$_2$ by flushing with Ar for 1 h, the catalyst was heated to 400 °C at 10 °C min^{-1} in an Ar flow (30 mL min^{-1}). An adsorption stoichiometry of H/Co = 1:1 was used to determine the number of surface metallic sites. The Co dispersion (D) was then calculated by the following equation

$$D = \frac{\text{moles of metallic Co atoms on surface}}{\text{moles of metallic Co atoms in sample}} \times 100\%$$

The mean particle size ($d_{\text{particles}}$, Å) was calculated based on the following equation

$$D = 6 \times \frac{v_{\text{m}}/a_{\text{m}}}{d_{\text{particles}}}$$

where a_m is the area occupied by a surface Co atom and v_m is the volume occupied by a Co atom in bulk metal. For face-centered cubic (fcc) Co, $a_m = 6.59$ Å^2 and $v_m = 11.00$ Å^3.[62]

2.5. Catalytic Testing. The catalytic behavior was investigated in a fixed-bed reactor. The gas flow is controlled by Books 5850E mass flow controllers (MFCs). The pressure is controlled *via* a back pressure regulator. First, 0.6 g of the catalyst was diluted with 1 mL of quartz powder (60−80 mesh). The as-synthesized samples (Ru$_1$/CoAl−O, Ru NPs/CoAl−O and CoAl−O) were reduced at 400 °C and 0.3 MPa H$_2$ for 6 h with an hourly gas space velocity (HGSV) of 2.0 L g^{-1} h^{-1} to transform into Ru$_1$Co$_n$ SAA, Ru/Co NPs, and Co NPs catalysts, respectively. After *in situ* reduction, the reactor was cooled to 50 °C, and syngas ($n_{H_2}/n_{CO} = 2$, GHSV = 2.0 L g^{-1} h^{-1}) was fed into the catalyst bed with the temperature increasing at a 2.0 °C min^{-1} heating rate. During testing, the pressure of the syngas was maintained at 2.0 MPa, and the reaction products passed a 130 °C hot trap and a 5 °C cooling trap at a working pressure. The composition of the reactants and tail gas were analyzed online *via* gas chromatography (GC). CO, CO$_2$, CH$_4$, and N$_2$ were analyzed by a carbon molecular sieve column and a TCD. The light hydrocarbons were analyzed using a capillary Porapak-Q column with a flame ionization detector (FID). The oil and wax were analyzed offline using GC with an OV-101 capillary column and an FID. The catalytic activity was determined as moles of CO converted to hydrocarbons per gram of metal per second. The hydrocarbon selectivities were calculated on a carbon basis. An average of 3% and a maximum of 5% mass and carbon balance errors were calculated for the run. The activity values (mol$_{CO}$ mol$_M^{-1}$ h^{-1}) were calculated by the equation

$$activity = F_{mh}C_v/n_M$$

where F_{mh} is the molar flow of CO (mol h^{-1}), C_v is the CO conversion in %, and n_M is the number of metallic Co and Ru atoms in the reactor in moles. The chain growth probability (α) was evaluated from the straight-line slopes determined by the following equation based on the C$_{10}$−C$_{24}$ products

$$W_n = n\alpha^{n-1}(1 - \alpha)^2$$

The environmental transmission electron microscopy (ETEM) test, X-ray absorption fine structure (XAFS) measurements and analysis details, computational details, and Fourier transform infrared (FTIR) spectra tests are described in the Supporting Information.

3. RESULTS AND DISCUSSION

3.1. Catalyst Synthesis and Characterization. LDHs are typical 2D functional materials with multimetal hydroxide layers and abundant interlayer anions.[63,64] Taking advantage of their unique layered structure, the Ru$_1$Co$_n$ SAA was prepared *via* a CoAl-LDH-based 2D space confinement strategy. As shown in Figure 1a, first, a coprecipitation method was used to prepare CoAl-(RuCl$_5^{2-}$)-LDHs, in which the RuCl$_5^{2-}$ ions with OH$^-$, CO$_3^{2-}$ and H$_2$O species were confined in the subnanometer 2D spaces between the electropositive CoAl hydroxide laminates. The interlayered anions with electrostatic repulsion can serve as a fence to prevent the agglomeration of RuCl$_5^{2-}$ species and assist in maintaining the atomic dispersion of Ru atoms in the following thermal reduction processes. The TEM image in Figure 1b shows the irregular nanosheet morphology of CoAl-(RuCl$_5^{2-}$)-LDHs with an ~3 nm
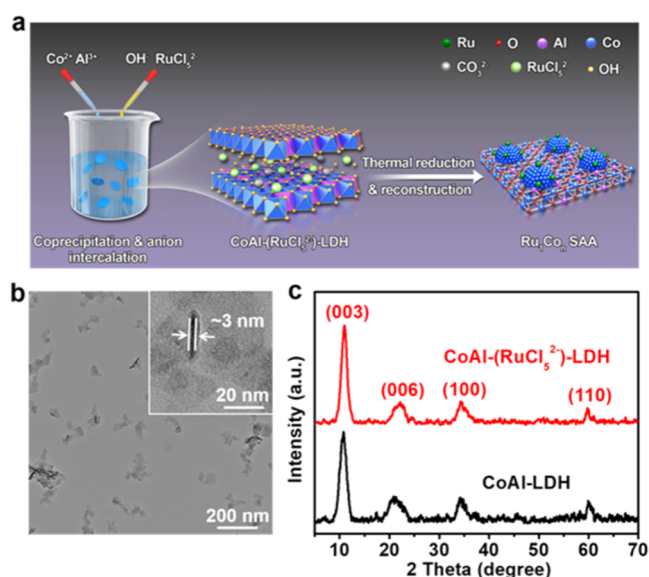

Figure 1. (a) Schematic illustration of the strategy of anion intercalation and 2D confinement to synthesize Ru$_1$Co$_n$ SAA. (b) TEM image of CoAl-(RuCl$_5^{2-}$)-LDHs. (c) PXRD patterns of CoAl-LDHs and CoAl-(RuCl$_5^{2-}$)-LDHs.

thickness. Their crystalline phase was demonstrated by the PXRD pattern (Figure 1c) with the characteristic (003), (006), (100), and (110) diffraction peaks of layered double hydroxides. The TEM and PXRD results are identical to those of CoAl-LDHs without RuCl$_5^{2-}$ addition (Figure S1), confirming the formation of 2D LDH nanosheets. The crystallographic thickness of a single-layer LDH is approximately 0.48 nm, and the interlayer distance of CoAl-LDH (NO$_3^-$) is approximately 0.89 nm, as reported in the literature.[65,66] Thus, our LDH samples contain approximately three crystallographic layers with two interlayers. Second, the CoAl-(RuCl$_5^{2-}$)-LDHs were reduced under an H$_2$ atmosphere at 400 °C to decompose the OH$^-$, CO$_3^{2-}$, and H$_2$O species and discharge them. Then, the LDH structure was transformed into an Al^{3+}-doped or substituted CoO phase (CoAl−O). Meanwhile, the ionic RuCl$_5^{2-}$ and some surface Co^{2+} ions were reduced to the metallic state, forming Ru$_1$Co$_n$ structures with isolated single-atom Ru anchored on the Co nanoparticle surface. It is worth mentioning that the metallic Ru and Co in the sample are liable to be oxidized by O$_2$ in air at room temperature, forming a high oxidation state sample (labeled Ru$_1$/CoAl−O). Thus, before FTS testing, the Ru$_1$/CoAl−O sample should be prereduced in H$_2$ at 400 °C to obtain Ru$_1$Co$_n$ SAA loaded on the CoAl−O substrate as the active FTS catalyst.

The structure of the Ru$_1$/CoAl−O precursor was characterized as shown in Figure 2. Figure 2a reveals that the morphology becomes more aggregate with irregular nanosheets or nanoparticles after the thermal reduction process. The lattice spacings of 2.33 and 2.11 Å in the HRTEM image of Ru$_1$/CoAl−O (Figure 2b) are close to, but slightly smaller than, those of the (111) and (200) planes of $Pm\overline{3}m$ cubic CoO (2.46 and 2.13 Å, respectively). These phenomena indicate the substitution of Al^{3+} ions into CoO crystals, leading to lattice contraction, as also confirmed by the PXRD results (Figure S2a). The corresponding fast Fourier transform (FFT) pattern (Figure 2c) oriented along the [220] Z-axis further reveals the simple cubic (sc) structure. In addition, no distinct brighter Ru
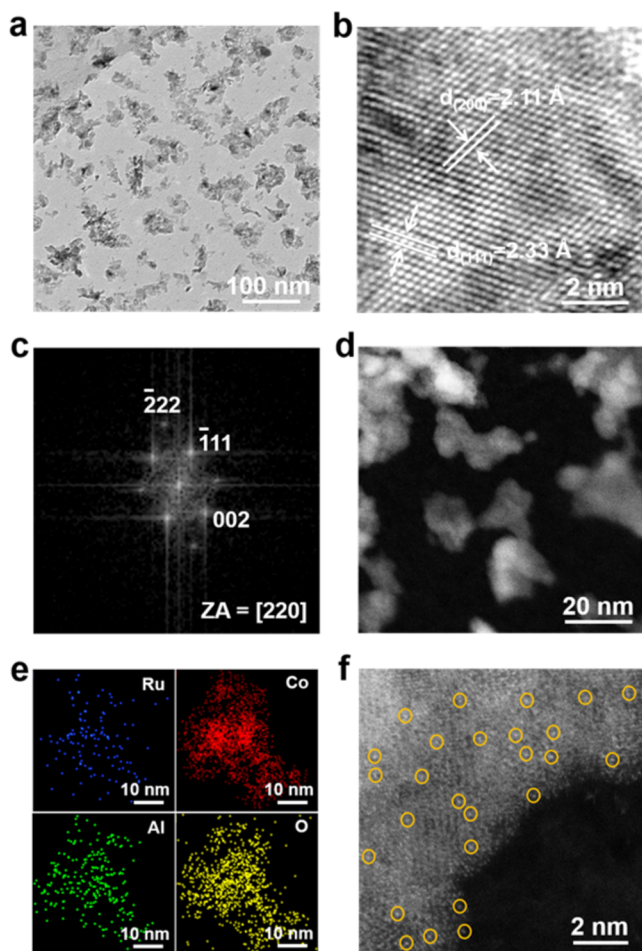
Figure 2. (a) TEM image, (b) HRTEM image, and (c) FFT pattern oriented along the [220] Z-axis of the $Ru_1/CoAl-O$ sample. (d) HAADF-STEM image and (e) element maps of Ru (blue), Co (red), Al (green), and O (yellow). (f) AC-HAADF-STEM image of $Ru_1/CoAl-O$.

Figure 3. (a) TPR results of Ru_1Co_n SAA, Ru/Co NPs, and Co NPs samples. *In situ* PXRD profiles of (b) Ru_1Co_n SAA, (c) Ru/Co NPs, and (d) Co NPs samples under H_2 reduction conditions. (e) Co 2p XPS spectra of the $Ru_1/CoAl-O$, Ru NPs/CoAl-O, and CoAl-O samples. (f) *In situ* Co 2p XPS spectra of Ru_1Co_n SAA, Ru/Co NPs, and Co NPs samples.

nanoparticles can be observed in the HAADF-STEM image (Figure 2d), and all of the Ru, Co, Al, and O elements are uniformly distributed, as demonstrated by the energy-dispersive X-ray spectroscopy analysis (EDXA) (Figures 2e and S2b). AC-HAADF-STEM was further used to discern the atomic structure of $Ru_1/CoAl-O$ (Figure 2f). Several atom-sized bright dots (Ru atoms) can be clearly distinguished on the CoAl-O matrix marked by orange circles. These results provide clear evidence of the existence of isolated Ru atoms on the surface of the CoAl-O substrate. The Ru content in $Ru_1/CoAl-O$ is 0.2 wt %, as measured by ICP-OES. In addition, Ru NPs/CoAl-O (Ru content: 0.32 wt %) (Figure S3a,b) and pure CoAl-O (Figure S3c) precursor samples were also synthesized for comparison, which showed similar surface areas and porosity properties to $Ru_1/CoAl-O$ *via* N_2 adsorption/desorption analysis (Figure S4).

TPR and a series of *in situ* techniques were performed to evaluate the thermal reduction behaviors of $Ru_1/CoAl-O$, Ru NPs/CoAl-O, and CoAl-O to Ru_1Co_n SAA, Ru/Co NPs, and Co NPs samples, respectively. As shown in the TPR profiles in Figure 3a, the three samples give similar reduction profiles. Two isolated peaks show the reduction of CoO to metallic Co (250–380 °C) and the reduction of CoAl compound oxide (550–750 °C). In addition, it can be noted that the addition of
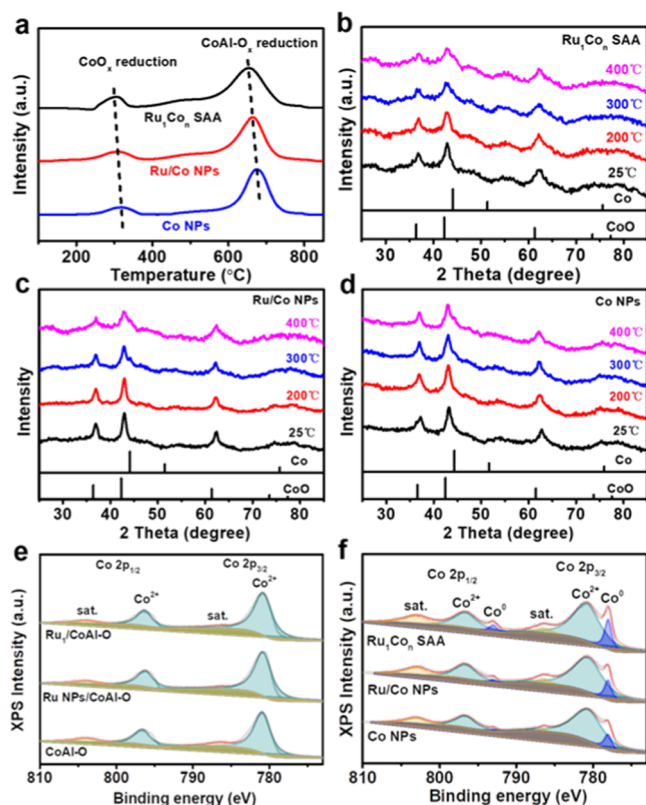
Ru single atoms or nanoparticles results in a shift in their reduction peaks to lower temperatures and enhances the area of the first reduction peak, compared to the Co NP sample. This phenomenon can be explained by the hydrogen spillover effect of Ru species for facilitating the reduction of the CoAl-O substrate.[33] To further elucidate the phase evolution of these samples during thermal reduction, an *in situ* PXRD study was performed under a hydrogen atmosphere at gradient temperatures. As shown in Figure 3b-d, at temperatures below 200 °C, all diffraction peaks of the three samples agree well with a right-shifted CoO phase (JCPDS no. 43-1004). This can be due to the substitution of Al^{3+} to Co^{2+} cation sites in the CoO lattice, thus causing lattice contraction. When the temperature is elevated to 300 and 400 °C, weak characteristic peaks corresponding to $Fm3m$ cubic Co (JCPDS no. 15-0806) emerge for all three samples, demonstrating the formation of metallic Co species. *Ex situ* and *in situ* XPS (Figures 3e,f and S5) were performed to investigate the surface chemical properties of those samples. The oxidation state of cobalt species in air at an ambient temperature is mainly 2+, as shown in Figure 3e. However, in the reductive H_2 environment at 400 °C, apart from the existence of Co^{2+} characteristic peaks, the observed peaks at 778.0 and 793.0 eV corresponding to metallic Co^0 (Figure 3f) indicate that some cobalt species in CoAl-O substrates were transformed into metallic Co^0 in the reduction process. The peak deconvolution results show that metallic Co^0 contributes 16.9, 12.0, and 11.5% of the Co 2p peaks' areas of the Ru_1Co_n SAA, Ru/Co NPs, and Co NPs

samples on the CoAl−O substrates, respectively (Table S1). To track the morphology evolution in the thermal reduction process, ETEM under an H_2 atmosphere was conducted on the Ru_1/CoAl−O sample (Figure 4). A similar mesoporous
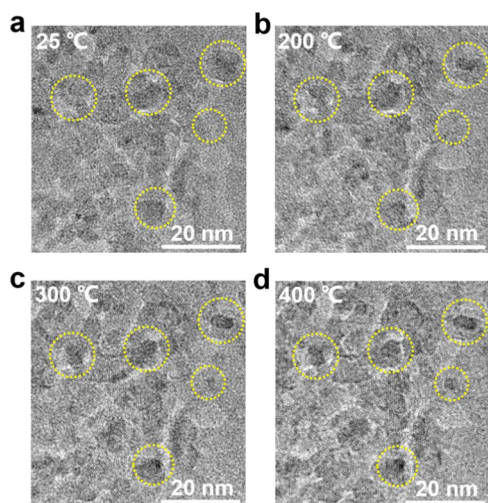

Figure 4. Representative TEM images from Ru_1/CoAl−O to Ru_1Co_n SAA in a H_2 atmosphere acquired at (a) 25 °C, (b) 200 °C, (c) 300 °C, and (d) 400 °C with ETEM.

nanosheet morphology can be observed in the representative images acquired at 25 and 200 °C. However, as the temperature is elevated to 300 or 400 °C, the surfaces become rougher and higher-contrast nanoparticles with a diameter of 6−8 nm emerge, as typically marked by orange circles. This phenomenon indicates the formation of metallic Co nanoparticles on the surface of CoAl−O, which agrees well with the TPR, *in situ* PXRD, and *in situ* XPS results.

H_2-TPD tests were performed to estimate the number of surface metal sites of the three catalysts (Figure S6). The corresponding metallic dispersion (D) and the size of the particles ($d_{particles}$) can be calculated based on the desorbed hydrogen amount from the H_2-TPD profiles and the DOR from the TPR results, as shown in Table 1. The observed

Table 1. ICP-OES, H_2-TPD, and TPR Data of the Catalysts

samples	Co loading (wt %)[a]	H_2 desorption (μmol $g_{cat.}^{-1}$)	DOR (%)[b]	dispersion (%)	$d_{particles}$ (nm)
Ru_1Co_n SAA	60.1	83.2	13.9	11.8	8.5
Ru/Co NPs	60.0	68.0	12.2	10.9	9.2
Co NPs	60.1	52.8	9.9	10.5	9.5

[a]Evaluated by ICP-OES. [b]Calculated from H_2-TPR results.

sequence of the hydrogen desorption amount is Ru_1Co_n SAA > Ru/Co NPs > Co NPs, which can be attributed to the enhanced reduction of Co *via* the hydrogen spillover effect of Ru. The smallest particle size (8.5 nm, close to the ETEM observation) and highest dispersion (11.8%) of Ru_1Co_n SAA indicate that single-atom Ru can facilitate the dispersion and stabilization of Co nanoparticles, which is consistent with previous reports.[20,29,30]

3.2. Catalytic Performance. The reduction and catalytic tests were performed in a fixed-bed reactor under typical industrial conditions. First, Ru_1/CoAl−O, Ru NPs/CoAl−O,

and CoAl−O samples were reduced at 400 °C for 6 h *via* H_2 to obtain the Ru_1Co_n SAA, Ru/Co NPs, and Co NPs catalysts, respectively. Then, catalytic tests were performed at a H_2/CO ratio of 2 and a pressure of 2.0 MPa. Table 2 shows the catalytic activity and hydrocarbon product distribution (expressed as C-mol% on a carbon basis) of the catalysts after 24 h of reaction. For all three catalysts, as the reaction temperature increases, the CO conversions increase distinctly. Ru_1Co_n SAA shows much higher CO conversions than Ru/Co NPs and Co NPs samples at any reaction temperature. More noteworthily, at a low temperature of 150 °C, Ru_1Co_n SAA shows a CO conversion of 12.5%, outstanding the counterparts of 5.6 and 3.1% for the Ru/Co NPs and Co NPs samples, respectively. The low reaction temperature (150 °C) reflects the extra high activity of this system. The activity of the Ru_1Co_n SAA (2.6 mol_{CO} mol_M^{-1} h^{-1}) is much higher than those of the Ru/Co NPs (1.3 mol_{CO} mol_M^{-1} h^{-1}) and Co NPs (0.9 mol_{CO} mol_M^{-1} h^{-1}) samples. More importantly, the turnover frequency (TOF, moles of CO converted per mol surface metallic atoms per second) value of the Ru_1Co_n SAA (6.1×10^{-3} s^{-1}) is 1.8 and 2.5 times those of the Ru/Co NPs (3.3×10^{-3} s^{-1}) and Co NPs (2.4×10^{-3} s^{-1}) samples at a reaction temperature of 150 °C, respectively. This result reveals that Ru single-atom sites in Ru_1Co_n SAA are more active than pure Ru and Co surfaces for FTS.

Another important requirement for an FTS catalyst is the maximum production of the heavy hydrocarbon fraction is obtained while suppressing the formation of methane to the lowest level possible. Considering the product distributions over the three catalysts, we determined that the FTS products can be tuned to higher molecular (C_{5^+}) weights by controlling the single-atom dispersion of Ru. At a low temperature of 150 °C, Ru_1Co_n SAA exhibits a high C_{5^+} selectivity of 86.0% and ultralow CO_2 and CH_4 selectivities of 0.2 and 3.5%, respectively. Nevertheless, Ru/Co NPs and Co NPs catalysts exhibit lower C_{5^+} selectivities of 81.3 and 77.7%, respectively, and their CO_2 and CH_4 selectivities are also much higher than those of the Ru_1Co_n SAA sample. When the reaction temperature increased to 200 °C, the C_{5^+} selectivity of Ru_1Co_n SAA was maintained at 86.3% with 0.2 and 5.7% CO_2 and CH_4, respectively. For the Ru/Co NPs and Co NPs catalysts, their C_{5^+} percentages decreased to 69.2 and 60.8%, and the CO_2 and CH_4 selectivities dramatically increased to 1.0 and 16.9% for the Ru/Co NPs and 1.7 and 24.6% for the Co NPs, respectively. To further confirm the effect of the Ru_1Co_n sites on product distribution, the Anderson−Schulz−Flory (ASF) distributions for C_{5^+} hydrocarbons were provided. Figure 5a shows the FTS product distributions over the three catalysts at a reaction temperature of 200 °C. Except for the observed increasing tendency toward the C_{5^+} selectivity from the Co NPs and the Ru/Co NPs to the Ru_1Co_n SAA samples, it can be seen that their maximal selectivities are located at C_7, C_8, and C_{12} for the three samples, respectively. This phenomenon indicates that Ru_1Co_n SAA can tune the selectivity of the FTS products to higher molecular weights. As shown in Figure 5b, the chain growth probability (α) values of the catalysts evaluated using C_{10}−C_{24} products increased from 0.63 of Co NPs to 0.72 of Ru/Co NPs and 0.76 of Ru_1Co_n SAA. This further reveals that Ru_1Co_n favors chain growth more than pure Co and Ru surfaces. These results indicate that the Ru single-atom sites on Ru_1Co_n SAA can not only improve the CO consumption rate but also favor chain growth, resulting in both a higher catalytic activity and a heavy

Table 2. Performance Comparison of the Ru_1Co_n SAA, Ru/Co NPs, and Co NPs Samples in FTS Testing[a]

catalyst	T (°C)	CO conv. (%)	activity (mol_{CO} mol_M^{-1} h^{-1})	TOF (10^{-3} s^{-1})	sel. (%)			
					CO_2	CH_4	C_{2-4}	C_5^+
Ru_1Co_n SAA	150	12.5	2.6	6.1	0.2	3.5	10.3	86.0
	180	37.9	7.8	18.3	0.2	5.5	10.1	84.2
	200	62.0	12.8	30.0	0.2	5.7	7.8	86.3
Ru/Co NPs	150	5.6	1.3	3.3	0.3	7.9	10.5	81.3
	180	18.5	4.2	10.7	0.7	12.5	11.7	75.1
	200	33.1	7.6	19.3	1.0	16.9	12.9	69.2
Co NPs	150	3.1	0.9	2.4	1.0	8.0	13.3	77.7
	180	11.2	3.3	8.8	1.5	17.0	13.4	68.1
	200	22.0	6.4	17.1	1.7	24.6	12.9	60.8

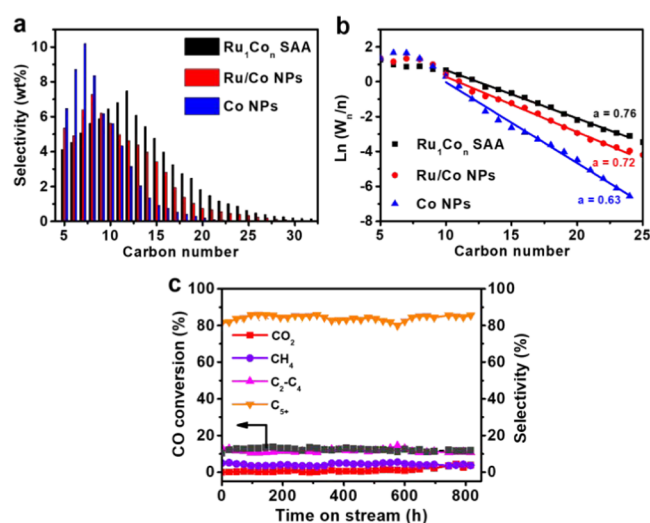[a]Fixed-bed reactor, 2.0 MPa, H_2/CO = 2/1, space velocity = 2.0 L g^{-1} h^{-1}.

Figure 5. (a) Distributions of the C_5^+ products of the Ru_1Co_n SAA, Ru/Co NPs, and Co NPs samples. (b) ASF distributions for the three catalysts. (c) Durability test of Ru_1Co_n SAA. The tests were performed under the conditions of 2.0 MPa, 2.0 L g_{cat}^{-1} h^{-1}, and 2/1 H_2/CO ratio.

hydrocarbon selectivity. To evaluate the activity and selectivity of Ru_1Co_n SAA, the recently reported Ru and Co-based materials for FTS were overviewed (Table S2), and the promising performance is clear. After the FTS test, the structures of the spent catalysts were also thoroughly characterized (Figures S7–S9), showing the good structural stability of Ru_1Co_n SAA. Moreover, this catalyst was subjected to an 816 h test at 150 °C for FTS (Figure 5c), during which the CO conversion and hydrocarbon selectivities on the stream underwent no significant changes. This demonstrates that Ru_1Co_n SAA is highly durable for FTS.

3.3. *In Situ* XAFS Studies of Ru_1Co_n SAA. To identify the local electronic and geometric structures of Ru atom sites and uncover their catalytic mechanism, the structural evolution of Ru species during the high-temperature reduction and FTS reaction on Ru_1Co_n SAA was investigated *via in situ* XAFS measurements. Details of the test and fitting methods are described in the Supporting Information. Figure 6a presents the *R*-space data of the k^2-weighted Ru K-edge Fourier transform (FT) extended X-ray absorption fine structure (EXAFS) spectra at different reduction stages, as well as during the FTS reaction. The corresponding FT EXAFS fitting results are shown in Figure S10 and Table S3. For the nonreduced Ru_1/CoAl−O sample at room temperature (∼25 °C) in an air atmosphere, a major peak corresponding to Ru−O coordina-
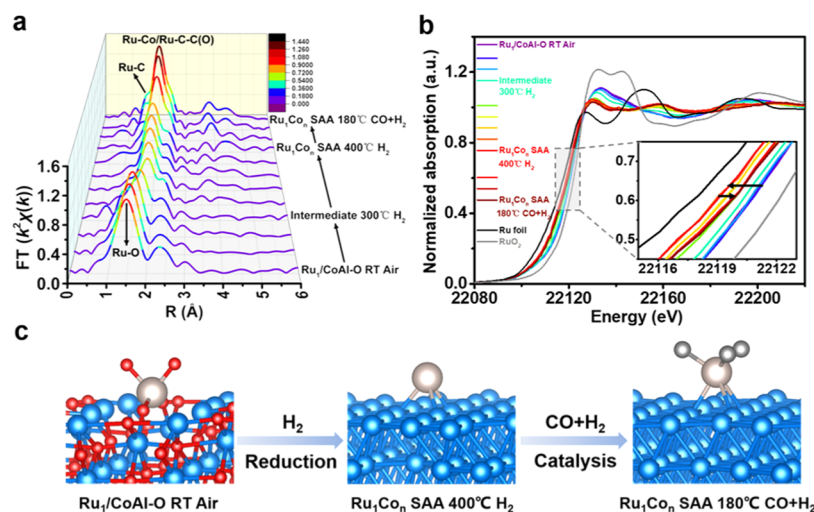

Figure 6. *In situ* XAFS measurements collected under different conditions on Ru_1Co_n SAA. (a) Ru K-edge FT EXAFS spectra and (b) Ru K-edge X-ray absorption near-edge structure (XANES) spectra. The plots are not corrected for phase shift. (c) Schematic structural evolution of the single-atom Ru site at different stages. The brown, red, blue, and gray balls represent Ru, O, Co, and C atoms, respectively.

tion is observed at ~1.5 Å. The FT EXAFS fitting results show that the coordination number (CN) of O atoms to a Ru atom is approximately 4.0, with a mean bond length of 2.05 Å. Moreover, the FT EXAFS of $Ru_1/CoAl-O$ also shows a minor signal at 2.4 Å. The best-fitting analysis clearly shows that this peak is satisfactorily interpreted as a Ru−O−Co contribution with a Ru−Co distance of 2.96 Å and a CN of 1.9. Together, these analyses reveal the isolated dispersion of Ru atoms with a $Ru-O_4-Co_2$ moiety, as shown in Figure 6c. The FT EXAFS spectra for $Ru_1/CoAl-O$ below 200 °C are very analogous, suggesting an unchanged local structure of the Ru species. Then, as the temperature increases to higher than 300 °C, the FT EXAFS data show a shift of the first nearest neighbor peak to a larger distance. The intensity of the major peak first descends and then rises, indicating that a phase transformation of the sample occurred during the reduction treatment in H_2. The FT EXAFS data remain unchanged after reaching 400 °C, and the peak for Ru−O disappears. The major peak at 1.9 Å could be attributed to the backscattering between the Ru and Co atoms. This suggests a reconstruction of single-atom Ru and its neighboring atoms, during which Ru−O bonds are ruptured and Ru−Co bonds are formed. The FT EXAFS fitting results of the Ru_1Co_n SAA sample after a 400 °C reduction in H_2 manifest that the Ru−Co CN is 3.0, showing an unsaturated coordinated environment of the Ru atoms. In addition, the Ru−Co bond length is 2.46 Å, which is significantly shorter than that of the RuCo alloys (2.56−2.58 Å),[67] indicating that Ru atoms bond to Co nanoparticles with strong electronic interactions. The best-fitting analyses for the minor peak at ~2.5 Å reveal that this peak could be attributed to the backscattering contribution between Ru and the second layer Co atoms with a bond length of 2.96 Å and a CN of 1.2. Thus, isolated Ru atoms in the Ru_1Co_n SAA sample are anchored on the Co nanoparticle surface with a definite coordination-unsaturated $Ru-Co_3$ structure, as shown in Figure 6c. Afterward, the temperature was decreased to 180 °C and the atmosphere was switched from H_2 to syngas (CO + H_2) to examine the chemical evolution of active Ru centers during the FTS reaction. As shown in Figure 6a, there is still no Ru−Ru bond formation under the reaction conditions, suggesting that these Ru atoms on the surface of Co nanoparticles retain single-atom dispersion during catalysis. A minor peak at ~1.5 Å can be clearly observed, which could be dominated by the Ru−C scattering path. This indicates the adsorption of some carbon-containing species on single-atom Ru sites during FTS. The quantitative fitting analyses show that the first-shell CN of Ru−C is 2.8, with a bond length of 2.01 Å. In addition, the intensity of the main peak at ~2.0 Å increases remarkably after syngas injection, which could be related to the increase in CN. The best-fitting analyses reveal that, except for the Ru−Co bonds with a CN of 3.4, the increase in this peak could be attributed to the backscattering contribution between Ru and the second layer C/O atoms (Ru−C−C(O)) with a bond length of 2.71 Å and a CN of 3.6. These results indicate that the single Ru atom in the $Ru-Co_3$ site would adsorb three C-containing species (CO or other C_nH_x species) when exposed to syngas under the FTS reaction, forming a sixfold coordination structure ($Ru-Co_3C_3$), as schematically shown in Figure 6c. It should be noted that the bond length of Ru−C (averaging 2.01 Å) is longer than that in ruthenium carbonyls ($Ru_3(CO)_{12}$, Ru−C bond length averaging 1.932 Å),[68] suggesting that the Ru−C bonds are weak and unstable. The generation of Ru−C intermediate

species during the FTS reaction was further confirmed by hydrogen treatment of the catalyst after the syngas tests, in which the Ru−C coordination peak disappeared, as shown in Figure S11a. These results reveal that single-atom Ru in Ru_1Co_n SAA can work as the active catalytic sites involved in the FTS reaction, in which three C species (C_1-C_n) can be adsorbed onto one Ru atom for the C−O rupture and chain growth reactions.

The oxidation state and electronic structure changes of single Ru atoms during the reduction and catalysis processes were further analyzed via X-ray absorption near-edge structure (XANES). Figure 6b presents the set of Ru K-edge XANES spectra recorded under different reduction and FTS reaction stages. It can be seen that the near-edge absorption energies (E_0) of the sample from all stages are located between those of RuO_2 and the Ru foil, implying the positively charged feature of single Ru atoms. It can be observed in the inset of Figure 6b that the XANES spectra below 200 °C are very similar, demonstrating the unchanged oxidation state of the Ru species, which agrees well with the in situ EXAFS results. Then, as the temperature increases from 300 to 400 °C, a distinct shift of the absorption edge toward a lower energy is observed, indicating the stepwise reduced oxidation state of Ru atoms. In comparison to metallic Ru foil, the electron deficiency of Ru atoms in Ru_1Co_n SAA after a 400 °C reduction is likely due to the electron transfer from Ru atoms to Co nanoparticles with strong electronic interactions. This further explains the shortened Ru−Co bond length (2.46 Å) and the outstanding structural stability of single-atom $Ru-Co_3$ sites. After switching to a syngas atmosphere at 180 °C, the absorption edge shifts to a higher energy. This phenomenon reveals the increased oxidation state of Ru atoms after adsorption of C species under FTS, as demonstrated by the in situ EXAFS results. In addition, as shown in Figure S11b, the hydrogen treatment of the catalyst after syngas tests can make the absorption edge shift to a lower energy, revealing the decreased oxidation state of the Ru atoms after desorption of the C species, which further confirms the generation of Ru−C intermediate species during the FTS reaction. The phenomenon of carrying positive charge for Ru atoms in $Ru-Co_3$ and $Ru-Co_3C_3$ structures is also well confirmed via DFT calculations (Figure S12). The lower electronic density over Ru is accompanied by an increase in the electronic density over Co in the Ru_1Co_n SAA, as confirmed by the XPS, FTIR CO adsorption, and DFT results, as shown in Figure S13. These results clearly show the formation of single-atom $Ru-Co_3$ active sites on Ru_1Co_n SAA from $Ru-O_4-Co_2$ sites on the CoAl−O substrate via H_2 reduction and demonstrate their $Ru-Co_3C_3$ configuration during FTS. In addition, the residual Cl in the sample was also measured via XRF analysis, and its possible effect on the electronic property and FTS performance of the Ru_1Co_n SAA is discussed in the Supporting Information.

3.4. DFT-Calculated FTS Mechanism. To further clarify the main factor that improves the catalytic performance of Ru_1Co_n SAA, DFT calculations were performed to investigate the FTS reaction mechanism that occurred on the Ru_1Co_n SAA, Co(111), and Ru(0001) surfaces. Generally, the reaction involves a sequence of steps, including adsorption and activation of CO and H_2, hydrogenation of CO to CH_x species, and chain growth processes. Initially, the reactants (CO and H_2) are adsorbed on the catalyst surface, followed by the formation of metal−C and metal−H bonds. It is worth mentioning that the most stable configuration before reaction

on Ru_1Co_n SAA is the structure of three CO molecules adsorbed onto a single Ru atom with one atomic H adsorbed onto the adjacent Co surface, as confirmed by the *in situ* EXAFS results. On Co(111) and Ru(0001), the initial state is the structure of a CO molecule and an atomic H adsorbed at the hollow sites of the metal surface. After adsorption, the conversion of CO to the C_n product occurs through a series of steps. The transition from CO to CH_x includes hydrogenation of CO to CHO (CO + H → HCO) and cleavage of the C−O bond (HCO → CH + O). On Ru_1Co_n SAA, after the hydrogenation of the CO molecule, the intermediate HCO adsorbs between the Ru and Co atoms. Finally, both CH and O adsorb on the Co surface, leaving two CO molecules on the Ru atom. For Co(111) and Ru(0001), the intermediate HCO adsorbs at the hollow site. To simplify the calculation, the transformation from CH to CH_x ($x \geq 2$) is not included. The transition-state energies 1 and 2 (TS1 and TS2) in Figure 7a
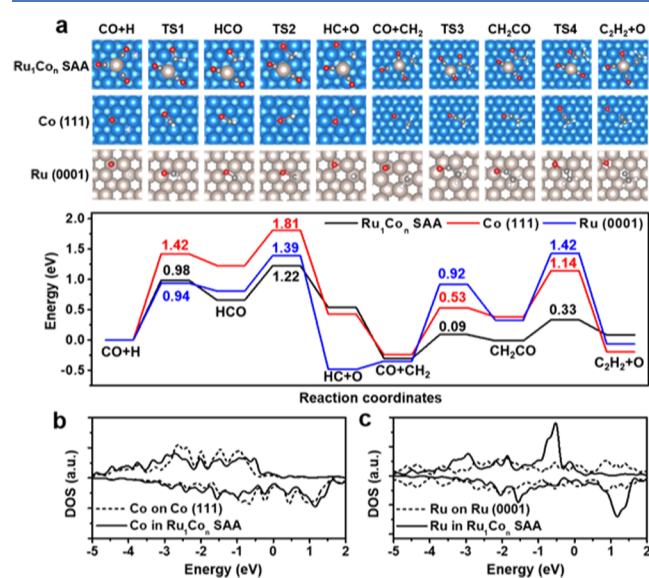

Figure 7. DFT calculation results over the Ru_1Co_n SAA, Co(111), and Ru(0001) surfaces. (a) Calculated reaction pathway on Ru_1Co_n SAA, Co(111), and Ru(0001) showing the conversion of CO to C_1 and C_2 products containing C−O bond breaking and C−C bond forming: the hydrogenation of adsorbed CO to CHO (CO + H → HCO) and the cleavage of the C−O bond (HCO → CH + O); the formation of the C−C bond (CO + CH_2 → CH_2CO) and the cleavage of the C−O bond (CH_2CO → C_2H_2 + O). Top: atomic structure at each stage; bottom: energy profile showing the related energies corresponding to the structures in the top panel. (b) Projected density of states (PDOS) on d orbitals of the surface Co atom on Co(111) (dashed line) and in Ru_1Co_n SAA that bonds to the Ru atom (solid line). (c) PDOS on d orbitals of the surface Ru atom on Ru(0001) (dashed line) and in Ru_1Co_n SAA (solid line).

indicate that, in all cases, the bottleneck of the entire process is the splitting of the C−O bond (TS2), which is consistent with previous studies.[69] Compared to 1.81 and 1.39 eV for the Co(111) and Ru(0001) surfaces, the Ru_1Co_n SAA system has the lowest reaction barrier (1.22 eV), resulting in the highest activity in the CO conversion.

In the chain growth process, two reaction mechanisms are proposed: a carbide mechanism and a CO insertion mechanism.[70] Herein, we only consider the CO insertion pathways, which are the most likely to occur on the Co surface according to previous studies.[71,72] From C_1 to C_2 products, the

C−C bond is formed (CO + CH_2 → CH_2CO) followed by the cleavage of the C−O bond (CH_2CO → C_2H_2 + O). On Ru_1Co_n SAA, the initial state is the structure of three CO molecules bonding to the Ru atom with a CH_2 species adsorbed on the hollow site of Co(111). The CH_2CO bonds to both Ru and Co, which is similar to the intermediate state in the first conversion of the CO to CH_x species. For Co(111) and Ru(0001), the intermediate CH_2CO adsorbs at the hollow site, followed by cleavage of the C−O bond. After that, the following step could be the hydrogenation of the C_2H_2 species or the transformation from C_2 to C_n. The transition-state energy from C_1 to C_2 on Ru_1Co_n SAA (0.33 eV) is much lower than that on pure Co(111) (1.14 eV) and Ru(0001) (1.42 eV). Thus, the formation of long carbon chains prefers to occur on Ru_1Co_n SAA at a low temperature, resulting in a much lower C_1 (CO_2 and CH_4) selectivity than those on Ru/ Co NPs and Co NPs samples.

To reveal the origin of the high catalytic activity of Ru_1Co_n SAA, we show the projected density of states (PDOS) in the Co(111), Ru(0001), and Ru_1Co_n SAA systems in Figure 7b,c. Figure 7b shows the similar PDOS of the Co atom in Co(111) and Ru_1Co_n SAA. However, as shown in Figure 7c, the PDOS of the Ru atom in Ru_1Co_n SAA shows a much higher electron density near the Fermi level, compared to that in Ru(0001). Thus, the atomic Ru has a much stronger interaction with the reactants, resulting in an enhanced catalytic performance.[73] In conclusion, we can infer that the single Ru atoms with a unique electron density state and the surrounding Co atoms in Ru_1Co_n SAA play a cooperative role in FTS catalysis, resulting in high catalytic activity and long-chain hydrocarbon selectivity.

4. CONCLUSIONS

In summary, a Ru_1Co_n SAA with a trace amount of single Ru atoms immobilized on Co nanoparticles was synthesized using an LDH-based anion intercalation and 2D space confinement strategy, which exhibited a high catalytic performance toward FTS. The formation process as well as the electronic and geometric structure of Ru_1Co_n SAA were thoroughly studied using AC-HAADF-STEM, *in situ* PXRD, *in situ* XPS, ETEM, *in situ* XAFS, FTIR CO adsorption technologies, *etc.* The correlation of the catalytic evaluation, *in situ* XAFS, and the DFT calculations demonstrates that the Ru_1Co_n interface is more active than those of pure Co and Ru surfaces. Both the C−O splitting and C−C augmentation processes in FTS can be promoted by the cooperative effect of Ru atoms with a high electronic density near the Fermi level and the adjacent Co atoms, resulting in a high CO conversion and a long-chain hydrocarbon selectivity. These results offer an effective strategy for preparing thermally stable SAAs for diverse reactions and provide insights into the feasibility of the atomic-level interface design to optimize the performance of industrial catalysts.

◼ ASSOCIATED CONTENT

Ⓢ Supporting Information

The Supporting Information is available free of charge at https://pubs.acs.org/doi/10.1021/acscatal.0c04162.

> Experimental methods of ETEM, XAFS, and FTIR CO adsorption tests; computational details; TEM, HRTEM, AC-HAADF-STEM, and EDXA mapping images; PXRD and EDXA patterns; N_2 adsorption−desorption iso- therms and pore size distribution curves; XPS and FTIR

CO spectra; H_2-TPD profiles; *in situ* XAFS and fitting results; DFT calculation results; FTS performances of Ru/Co-based catalysts in the literature; and further discussion (PDF)

■ AUTHOR INFORMATION

Corresponding Authors

   Yu Wang − *Shanghai Synchrotron Radiation Facility, Shanghai Advanced Research Institute, Chinese Academy of Sciences, Shanghai 201204, China*; Email: wangyu@ sinap.ac.cn

   Jiangang Chen − *State Key Laboratory of Coal Conversion, Institute of Coal Chemistry, Chinese Academy of Sciences, Taiyuan 030001, Shanxi, China*; Email: chenjg@ sxicc.ac.cn

   Yadong Li − *Department of Chemistry, Tsinghua University, Beijing 100084, China*; ⓘ orcid.org/0000-0003-1544-1127; Email: ydli@mail.tsinghua.edu.cn

Authors

   Ge Meng − *Department of Chemistry, Tsinghua University, Beijing 100084, China*

   Jiaqiang Sun − *State Key Laboratory of Coal Conversion, Institute of Coal Chemistry, Chinese Academy of Sciences, Taiyuan 030001, Shanxi, China; School of Chemical Engineering, University of Chinese Academy of Sciences, Beijing 100049, China*; ⓘ orcid.org/0000-0002-1673-7782

   Lei Tao − *Institute of Physics & University of Chinese Academy of Sciences, Chinese Academy of Sciences, Beijing 100190, China*

   Kaiyue Ji − *Department of Chemistry, Tsinghua University, Beijing 100084, China*

   Pengfei Wang − *State Key Laboratory of Coal Conversion, Institute of Coal Chemistry, Chinese Academy of Sciences, Taiyuan 030001, Shanxi, China*

   Xiaohui Sun − *Department of Chemistry, Tsinghua University, Beijing 100084, China*

   Tingting Cui − *Department of Chemistry, Tsinghua University, Beijing 100084, China*

   Shixuan Du − *Institute of Physics & University of Chinese Academy of Sciences, Chinese Academy of Sciences, Beijing 100190, China; CAS Center for Excellence in Topological Quantum Computation, University of Chinese Academy of Sciences, Beijing 100190, China*; ⓘ orcid.org/0000-0001-9323-1307

   Dingsheng Wang − *Department of Chemistry, Tsinghua University, Beijing 100084, China*; ⓘ orcid.org/0000-0003-0074-7633

Complete contact information is available at:
https://pubs.acs.org/10.1021/acscatal.0c04162

Author Contributions

∇G.M., J.S., and L.T. contributed equally to this work.

Notes

The authors declare no competing financial interest.

■ REFERENCES

(1) Khodakov, A. Y.; Chu, W.; Fongarland, P. Advances in the development of novel cobalt Fischer-Tropsch catalysts for synthesis of long-chain hydrocarbons and clean fuels. *Chem. Rev.* **2007**, *107*, 1692−1744.

(2) de Smit, E.; Weckhuysen, B. M. The renaissance of iron-based Fischer-Tropsch synthesis: on the multifaceted catalyst deactivation behaviour. *Chem. Soc. Rev.* **2008**, *37*, 2758−2781.

(3) Wang, H.; Zhou, W.; Liu, J.; Si, R.; Sun, G.; Zhong, M.; Su, H.; Zhao, H.; Rodriguez, J. A.; Pennycook, S. J.; Idrobo, J. C.; Li, W.; Kou, Y.; Ma, D. Platinum-modulated cobalt nanocatalysts for low-temperature aqueous-phase Fischer-Tropsch synthesis. *J. Am. Chem. Soc.* **2013**, *135*, 4149−4158.

(4) Xie, C.; Niu, Z.; Kim, D.; Li, M.; Yang, P. Surface and interface control in nanoparticle catalysis. *Chem. Rev.* **2020**, *120*, 1184−1249.

(5) Zhong, L.; Yu, F.; An, Y.; Zhao, Y.; Sun, Y.; Li, Z.; Lin, T.; Lin, Y.; Qi, X.; Dai, Y.; Gu, L.; Hu, J.; Jin, S.; Shen, Q.; Wang, H. Cobalt carbide nanoprisms for direct production of lower olefins from syngas. *Nature* **2016**, *538*, 84−87.

(6) Jiao, F.; Li, J.; Pan, X.; Xiao, J.; Li, H.; Ma, H.; Wei, M.; Pan, Y.; Zhou, Z.; Li, M.; Miao, S.; Li, J.; Zhu, Y.; Xiao, D.; He, T.; Yang, J.; Qi, F.; Fu, Q.; Bao, X. Selective conversion of syngas to light olefins. *Science* **2016**, *351*, 1065−1068.

(7) Li, N.; Jiao, F.; Pan, X.; Chen, Y.; Feng, J.; Li, G.; Bao, X. High-quality gasoline directly from syngas by dual metal oxide-zeolite (OX-ZEO) catalysis. *Angew. Chem., Int. Ed.* **2019**, *58*, 7400−7404.

(8) Zhang, C.; Guo, X.; Yuan, Q.; Zhang, R.; Chang, Q.; Li, K.; Xiao, B.; Liu, S.; Ma, C.; Liu, X.; Xu, Y.; Wen, X.; Yang, Y.; Li, Y. Ethyne-reducing metal-organic frameworks to control fabrications of core/shell nanoparticles as catalysts. *ACS Catal.* **2018**, *8*, 7120−7130.

(9) Rahmati, M.; Safdari, M.-S.; Fletcher, T. H.; Argyle, M. D.; Bartholomew, C. H. Chemical and thermal sintering of supported metals with emphasis on cobalt catalysts during Fischer-Tropsch synthesis. *Chem. Rev.* **2020**, *120*, 4455−4533.

(10) Xie, C.; Chen, C.; Yu, Y.; Su, J.; Li, Y.; Somorjai, G. A.; Yang, P. Tandem catalysis for CO_2 hydrogenation to C_2-C_4 Hydrocarbons. *Nano Lett.* **2017**, *17*, 3798−3802.

(11) Li, J.; He, Y.; Tan, L.; Zhang, P.; Peng, X.; Oruganti, A.; Yang, G.; Abe, H.; Wang, Y.; Tsubaki, N. Integrated tuneable synthesis of liquid fuels via Fischer-Tropsch technology. *Nat. Catal.* **2018**, *1*, 787−793.

(12) Chang, Q.; Zhang, C.; Liu, C.; Wei, Y.; Cheruvathur, A. V.; Dugulan, A. I.; Niemantsverdriet, J. W.; Liu, X.; He, Y.; Qing, M.; Zheng, L.; Yun, Y.; Yang, Y.; Li, Y. Relationship between iron carbide phases (epsilon-Fe_2C, Fe_7C_3, and χ-Fe_5C_2) and catalytic performances of Fe/SiO_2 Fischer-Tropsch catalysts. *ACS Catal.* **2018**, *8*, 3304−3316.

(13) Tsakoumis, N. E.; Walmsley, J. C.; Ronning, M.; van Beek, W.; Rytter, E.; Hohnen, A. Evaluation of reoxidation thresholds for γ-Al_2O_3-supported cobalt catalysts under Fischer-Tropsch synthesis conditions. *J. Am. Chem. Soc.* **2017**, *139*, 3706−3715.

(14) Calderone, V. R.; Shiju, N. R.; Curulla-Ferre, D.; Chambrey, S.; Khodakov, A.; Rose, A.; Thiessen, J.; Jess, A.; Rothenberg, G. De novo design of nanostructured iron-cobalt Fischer-Tropsch catalysts. *Angew. Chem., Int. Ed.* **2013**, *52*, 4397−4401.

(15) Peng, X.; Cheng, K.; Kang, J.; Gu, B.; Yu, X.; Zhang, Q.; Wang, Y. Impact of hydrogenolysis on the selectivity of the Fischer-Tropsch synthesis: Diesel fuel production over mesoporous zeolite-Y-

supported cobalt nanoparticles. *Angew. Chem., Int. Ed.* **2015**, *54*, 4553−4556.

(16) Hibbitts, D. D.; Loveless, B. T.; Neurock, M.; Iglesia, E. Mechanistic role of water on the rate and selectivity of Fischer-Tropsch synthesis on ruthenium catalysts. *Angew. Chem., Int. Ed.* **2013**, *52*, 12273−12278.

(17) Kang, J.; Cheng, K.; Zhang, L.; Zhang, Q.; Ding, J.; Hua, W.; Lou, Y.; Zhai, Q.; Wang, Y. Mesoporous zeolite-supported ruthenium nanoparticles as highly selective Fischer-Tropsch catalysts for the production of C_5-C_{11} isoparaffins. *Angew. Chem., Int. Ed.* **2011**, *50*, 5200−5203.

(18) Eslava, J. L.; Iglesias-Juez, A.; Agostini, G.; Fernandez-Garcia, M.; Guerrero-Ruiz, A.; Rodriguez-Ramos, I. Time-Resolved XAS investigation of the local environment and evolution of oxidation states of a Fischer-Tropsch Ru-Cs/C catalyst. *ACS Catal.* **2016**, *6*, 1437−1445.

(19) Böller, B.; Durner, K. M.; Wintterlin, J. The active sites of a working Fischer-Tropsch catalyst revealed by operando scanning tunnelling microscopy. *Nat. Catal.* **2019**, *2*, 1027−1034.

(20) Bertella, F.; Lopes, C. W.; Foucher, A. C.; Agostini, G.; Concepción, P.; Stach, E. A.; Martínez, A. Insights into the promotion with Ru of Co/TiO$_2$ Fischer-Tropsch catalysts: An in situ spectroscopic study. *ACS Catal.* **2020**, *11*, 6042−6057.

(21) Bezemer, G. L.; Bitter, J. H.; Kuipers, H. P. C. E.; Oosterbeek, H.; Holewijn, J. E.; Xu, X.; Kapteijn, F.; van Dillen, A. J.; de Jong, K. P. Cobalt particle size effects in the Fischer-Tropsch reaction studied with carbon nanofiber supported catalysts. *J. Am. Chem. Soc.* **2006**, *128*, 3956−3964.

(22) den Breejen, J. P.; Radstake, P. B.; Bezemer, G. L.; Bitter, J. H.; Froseth, V.; Holmen, A.; de Jong, K. P. On the origin of the cobalt particle size effects in Fischer-Tropsch catalysis. *J. Am. Chem. Soc.* **2009**, *131*, 7197−7203.

(23) Sun, X.; Suarez, A. I. O.; Meijerink, M.; van Deelen, T.; Ould-Chikh, S.; Zecevic, J.; de Jong, K. P.; Kapteijn, F.; Gascon, J. Manufacture of highly loaded silica-supported cobalt Fischer-Tropsch catalysts from a metal organic framework. *Nat. Commun.* **2017**, *8*, No. 1680.

(24) Ralston, W. T.; Melaet, G.; Saephan, T.; Somorjai, G. A. Evidence of structure sensitivity in the Fischer-Tropsch reaction on model cobalt nanoparticles by time-resolved chemical transient kinetics. *Angew. Chem., Int. Ed.* **2017**, *56*, 7415−7419.

(25) Kang, J.; Zhang, S.; Zhang, Q.; Wang, Y. Ruthenium nanoparticles supported on carbon nanotubes as efficient catalysts for selective conversion of synthesis gas to diesel fuel. *Angew. Chem., Int. Ed.* **2009**, *48*, 2565−2568.

(26) Xiao, C. X.; Cai, Z. P.; Wang, T.; Kou, Y.; Yan, N. Aqueous-phase Fischer-Tropsch synthesis with a ruthenium nanocluster catalyst. *Angew. Chem., Int. Ed.* **2008**, *47*, 746−749.

(27) Cheng, Q.; Tian, Y.; Lyu, S.; Zhao, N.; Ma, K.; Ding, T.; Jiang, Z.; Wang, L.; Zhang, J.; Zheng, L.; Gao, F.; Dong, L.; Tsubaki, N.; Li, X. Confined small-sized cobalt catalysts stimulate carbon-chain growth reversely by modifying ASF law of Fischer-Tropsch synthesis. *Nat. Commun.* **2018**, *9*, No. 3250.

(28) Ellis, P. R.; Enache, D. I.; James, D. W.; Jones, D. S.; Kelly, G. J. A robust and precious metal-free high performance cobalt Fischer-Tropsch catalyst. *Nat. Catal.* **2019**, *2*, 623−631.

(29) Girardon, J. S.; Quinet, E.; Griboval-Constant, A.; Chernavskii, P. A.; Gengembre, L.; Khodakov, A. Y. Cobalt dispersion, reducibility, and surface sites in promoted silica-supported Fischer-Tropsch catalysts. *J. Catal.* **2007**, *248*, 143−157.

(30) Diehl, F.; Khodakov, A. Y. Promotion of cobalt Fischer-Tropsch catalysts with noble metals: a review. *Oil Gas Sci. Technol.* **2009**, *64*, 11−24.

(31) Beaumont, S. K.; Alayoglu, S.; Specht, C.; Michalak, W. D.; Pushkarev, V. V.; Guo, J.; Kruse, N.; Somorjai, G. A. Combining in situ NEXAFS spectroscopy and CO$_{(2)}$ methanation kinetics to study Pt and Co nanoparticle catalysts reveals key insights into the role of platinum in promoted cobalt catalysis. *J. Am. Chem. Soc.* **2014**, *136*, 9898−9901.

(32) Hong, J.; Marceau, E.; Khodakov, A. Y.; Gaberova, L.; Griboval-Constant, A.; Girardon, J. S.; La Fontaine, C.; Briois, V. Speciation of ruthenium as a reduction promoter of silica-supported Co catalysts: A time-resolved in situ XAS investigation. *ACS Catal.* **2015**, *5*, 1273−1282.

(33) Phaahlamohlaka, T. N.; Kumi, D. O.; Dlamini, M. W.; Forbes, R.; Jewell, L. L.; Billing, D. G.; Coville, N. J. Effects of Co and Ru intimacy in Fischer-Tropsch catalysts using hollow carbon sphere supports: Assessment of the hydrogen spillover processes. *ACS Catal.* **2017**, *7*, 1568−1578.

(34) Hong, J.; Chu, W.; Chernavskii, P. A.; Khodakov, A. Y. Cobalt species and cobalt-support interaction in glow discharge plasma-assisted Fischer-Tropsch catalysts. *J. Catal.* **2010**, *273*, 9−17.

(35) Harmel, J.; Peres, L.; Estrader, M.; Berliet, A.; Maury, S.; Fecant, A.; Chaudret, B.; Serp, P.; Soulantica, K. hcp-Co nanowires grown on metallic foams as catalysts for Fischer-Tropsch synthesis. *Angew. Chem., Int. Ed.* **2018**, *57*, 10579−10583.

(36) Liu, J.; Su, H.; Sun, D.; Zhang, B.; Li, W. Crystallographic dependence of CO activation on cobalt catalysts: HCP versus FCC. *J. Am. Chem. Soc.* **2013**, *135*, 16284−16287.

(37) Karaca, H.; Safonova, O. V.; Chambrey, S.; Fongarland, P.; Roussel, P.; Griboval-Constant, A.; Lacroix, M.; Khodakov, A. Y. Structure and catalytic performance of Pt-promoted alumina-supported cobalt catalysts under realistic conditions of Fischer-Tropsch synthesis. *J. Catal.* **2011**, *277*, 14−26.

(38) Enache, D. I.; Rebours, B.; Roy-Auberger, M.; Revel, R. In situ XRD study of the influence of thermal treatment on the character-istics and the catalytic properties of cobalt-based Fischer-Tropsch catalysts. *J. Catal.* **2002**, *205*, 346−353.

(39) Li, W.; Liu, J.; Gu, J.; Zhou, W.; Yao, S.; Si, R.; Guo, Y.; Su, H.; Yan, C.; Li, W.; Zhang, Y.; Ma, D. Chemical insights into the design and development of face-centered cubic ruthenium catalysts for Fischer-Tropsch synthesis. *J. Am. Chem. Soc.* **2017**, *139*, 2267−2276.

(40) Marcinkowski, M. D.; Darby, M. T.; Liu, J.; Wimble, J. M.; Lucci, F. R.; Lee, S.; Michaelides, A.; Flytzani-Stephanopoulos, M.; Stamatakis, M.; Sykes, E. C. H. Pt/Cu single-atom alloys as coke-resistant catalysts for efficient C-H activation. *Nat. Chem.* **2018**, *10*, 325.

(41) Zhang, X.; Cui, G.; Feng, H.; Chen, L.; Wang, H.; Wang, B.; Zhang, X.; Zheng, L.; Hong, S.; Wei, M. Platinum-copper single atom alloy catalysts with high performance towards glycerol hydrogenolysis. *Nat. Commun.* **2019**, *10*, No. 5812.

(42) Chen, L.; Hou, K.; Liu, Y.; Qi, Z.; Zheng, Q.; Lu, Y. H.; Chen, J.; Chen, J. L.; Pao, C. W.; Wang, S.; Li, Y.; Xie, S.; Liu, F.; Prendergast, D.; Klebanoff, L. E.; Stavila, V.; Allendorf, M. D.; Guo, J.; Zheng, L.; Su, J.; Somorjai, G. A. Efficient hydrogen production from methanol using a single-site Pt1/CeO$_2$ Catalyst. *J. Am. Chem. Soc.* **2019**, *141*, 17995−17999.

(43) DeRita, L.; Resasco, J.; Dai, S.; Boubnov, A.; Thang, H. V.; Hoffman, A. S.; Ro, I.; Graham, G. W.; Bare, S. R.; Pacchioni, G.; Pan, X.; Christopher, P. Structural evolution of atomically dispersed Pt catalysts dictates reactivity. *Nat. Mater.* **2019**, *18*, 746−751.

(44) Liu, J.; Lucci, F. R.; Yang, M.; Lee, S.; Marcinkowski, M. D.; Therrien, A. J.; Williams, C. T.; Sykes, E. C. H.; Flytzani-Stephanopoulos, M. Tackling CO poisoning with single-atom alloy catalysts. *J. Am. Chem. Soc.* **2016**, *138*, 6396−6399.

(45) Li, X.; Rong, H.; Zhang, J.; Wang, D.; Li, Y. Modulating the local coordination environment of single-atom catalysts for enhanced catalytic performance. *Nano Res.* **2020**, *13*, 1842−1855.

(46) Tian, S.; Hu, M.; Xu, Q.; Gong, W.; Chen, W.; Yang, J.; Zhu, Y.; Chen, C.; He, J.; Liu, Q.; Zhao, H.; Wang, D.; Li, Y. Single-atom Fe with Fe$_1$N$_3$ structure showing superior performances for both hydrogenation and transfer hydrogenation of nitrobenzene. *Sci. China Mater.* **2020**, DOI: 10.1007/s40843-020-1443-8.

(47) Zhao, K.; Nie, X.; Wang, H.; Chen, S.; Quan, X.; Yu, H.; Choi, W.; Zhang, G.; Kim, B.; Chen, J. G. Selective electroreduction of CO$_2$ to acetone by single copper atoms anchored on N-doped porous carbon. *Nat. Commun.* **2020**, *11*, No. 2455.

(48) Sun, T.; Xu, L.; Wang, D.; Li, Y. Metal organic frameworks derived single atom catalysts for electrocatalytic energy conversion. *Nano Res.* **2019**, *12*, 2067−2080.

(49) Duchesne, P. N.; Li, Z.; Deming, C. P.; Fung, V.; Zhao, X.; Yuan, J.; Regier, T.; Aldalbahi, A.; Almarhoon, Z.; Chen, S.; Jiang, D.; Zheng, N.; Zhang, P. Golden single-atomic-site platinum electrocatalysts. *Nat. Mater.* **2018**, *17*, 1033−1039.

(50) Lee, B. H.; Park, S.; Kim, M.; Sinha, A. K.; Lee, S. C.; Jung, E.; Chang, W. J.; Lee, K. S.; Kim, J. H.; Cho, S. P.; Kim, H.; Nam, K. T.; Hyeon, T. Reversible and cooperative photoactivation of single-atom Cu/TiO$_2$ photocatalysts. *Nat. Mater.* **2019**, *18*, 620−626.

(51) Greiner, M. T.; Jones, T. E.; Beeg, S.; Zwiener, L.; Scherzer, M.; Girgsdies, F.; Piccinin, S.; Armbruster, M.; Knop-Gericke, A.; Schlogl, R. Free-atom-like d states in single-atom alloy catalysts. *Nat. Chem.* **2018**, *10*, 1008−1015.

(52) Zhang, J.; Zheng, C.; Zhang, M.; Qiu, Y.; Xu, Q.; Cheong, W. C.; Chen, W.; Zheng, L.; Gu, L.; Hu, Z.; Wang, D.; Li, Y. Controlling N-doping type in carbon to boost single-atom site Cu catalyzed transfer hydrogenation of quinolone. *Nano Res.* **2020**, *13*, 3082−3087.

(53) Lee, S. H.; Kim, J.; Chung, D. Y.; Yoo, J. M.; Lee, H. S.; Kim, M. J.; Mun, B. S.; Kwon, S. G.; Sung, Y. E.; Hyeon, T. Design principle of Fe-N-C electrocatalysts: How to optimize multimodal porous structures? *J. Am. Chem. Soc.* **2019**, *141*, 2035−2045.

(54) Wang, A.; Li, J.; Zhang, T. Heterogeneous single-atom catalysis. *Nat. Rev. Chem.* **2018**, *2*, 65−81.

(55) Yang, J.; Li, W.; Wang, D.; Li, Y. Single-atom materials: Small structures determine macroproperties. *Small Struct.* **2020**, No. 2000051.

(56) Liu, L.; Corma, A. Metal catalysts for heterogeneous catalysis: From single atoms to nanoclusters and nanoparticles. *Chem. Rev.* **2018**, *118*, 4981−5079.

(57) Zhuang, Z.; Kang, Q.; Wang, D.; Li, Y. Single-atom catalysis enables long-life, high-energy lithium-sulfur batteries. *Nano Res.* **2020**, *13*, 1856−1866.

(58) Hannagan, R. T.; Giannakakis, G.; Flytzani-Stephanopoulos, M.; Sykes, E. C. H. Single-atom alloy catalysis. *Chem. Rev.* **2020**, *120*, 12044−12088.

(59) Zhang, N.; Ye, C.; Yan, H.; Li, L.; He, H.; Wang, D.; Li, Y. Single-atom site catalysts for environmental catalysis. *Nano Res.* **2020**, *13*, 3165−3182.

(60) Zhou, D.; Cai, Z.; Bi, Y.; Tian, W.; Luo, M.; Zhang, Q.; Zhang, Q.; Xie, Q.; Wang, J.; Li, Y.; Kuang, Y.; Duan, X.; Bajdich, M.; Siahrostami, S.; Sun, X. Effects of redox-active interlayer anions on the oxygen evolution reactivity of NiFe-layered double hydroxide nanosheets. *Nano Res.* **2018**, *11*, 1358−1368.

(61) Shen, J.; Yin, X.; Karpuzov, D.; Semagina, N. PVP-stabilized mono- and bimetallic Ru nanoparticles for selective ring opening. *Catal. Sci. Technol.* **2013**, *3*, 208−221.

(62) Hall, W. K.; Spiewak, B. E.; Cortright, R. D.; Dumesic, J. A.; Knözinger, H.; Pfeifer, H.; Kazansky, V. B.; Bond, G. C. Characterization of Solid Catalysts. In *Handbook of Heterogeneous Catalysis*; Ertl, G.; Knözinger, H.; Weitkamp, J., Eds.; Wiley-VCH: Weinheim, Germany, 1997; pp 689−770.

(63) Fan, G.; Li, F.; Evans, D. G.; Duan, X. Catalytic applications of layered double hydroxides: recent advances and perspectives. *Chem. Soc. Rev.* **2014**, *43*, 7040−7066.

(64) Feng, J.; He, Y.; Liu, Y.; Du, Y.; Li, D. Supported catalysts based on layered double hydroxides for catalytic oxidation and hydrogenation: general functionality and promising application prospects. *Chem. Soc. Rev.* **2015**, *44*, 5291−5319.

(65) Ping, J.; Wang, Y.; Lu, Q.; Chen, B.; Chen, J.; Huang, Y.; Ma, Q.; Tan, C.; Yang, J.; Cao, X.; Wang, Z.; Wu, J.; Ying, Y.; Zhang, H. Self-assembly of single-layer CoAl-layered double hydroxide nanosheets on 3D graphene network used as highly efficient electrocatalyst for oxygen evolution reaction. *Adv. Mater.* **2016**, *28*, 7640−7645.

(66) Liu, Z.; Ma, R.; Osada, M.; Iyi, N.; Ebina, Y.; Takada, K.; Sasaki, T. Synthesis, anion exchange, and delamination of Co-Al layered double hydroxide: Assembly of the exfoliated nanosheet/

polyanion composite films and magneto-optical studies. *J. Am. Chem. Soc.* **2006**, *128*, 4872−4880.

(67) Mao, J.; Chen, W.; Sun, W.; Chen, Z.; Pei, J.; He, D.; Lv, C.; Wang, D.; Li, Y. Rational control of the selectivity of a ruthenium catalyst for hydrogenation of 4-nitrostyrene by strain regulation. *Angew. Chem., Int. Ed.* **2017**, *56*, 11971−11975.

(68) Churchill, M. R.; Hollander, F. J.; Hutchinson, J. P. An accurate redetermination of the structure of triruthenium dodecacarbonyl, Ru$_3$(CO)$_{12}$. *Inorg. Chem.* **1977**, *16*, 2655−2659.

(69) Shetty, S.; van Santen, R. A. CO dissociation on Ru and Co surfaces: The initial step in the Fischer-Tropsch synthesis. *Catal. Today* **2011**, *171*, 168−173.

(70) Rofer-DePoorter, C. K. A comprehensive mechanism for the Fischer-Tropsch synthesis. *Chem. Rev.* **1981**, *81*, 447−474.

(71) Chen, C.; Wang, Q.; Wang, G.; Hou, B.; Jia, L.; Li, D. Mechanistic insight into the C$_2$ hydrocarbons formation from syngas on fcc-Co(111) surface: A DFT study. *J. Phys. Chem. C* **2016**, *120*, 9132−9147.

(72) Zhuo, M.; Tan, K. F.; Borgna, A.; Saeys, M. Density functional theory study of the CO insertion mechanism for Fischer-Tropsch synthesis over Co catalysts. *J. Phys. Chem. C* **2009**, *113*, 8357−8365.

(73) Nørskov, J. K.; Bligaard, T.; Rossmeisl, J.; Christensen, C. H. Towards the computational design of solid catalysts. *Nat. Chem.* **2009**, *1*, 37−46.